ARTICLE

Check for updates

Impact of solid-electrolyte interphase reformation on capacity loss in silicon-based lithium-ion batteries

T. Vorauer [1,5], J. Schöggl[1,5], S. G. Sanadhya[2], M. Poluektov[2], W. D. Widanage [2], L. Figiel [2], S. Schädler [3], B. Tordoff[3], B. Fuchsbichler[4], S. Koller[4] & R. Brunner [1✉]

High-density silicon composite anodes show large volume changes upon charging/discharging triggering the reformation of the solid electrolyte interface (SEI), an interface initially formed at the silicon surface. The question remains how the reformation process and accompanied material evolution, in particular for industrial up-scalable cells, impacts cell performance. Here, we develop a correlated workflow incorporating X-ray microscopy, field-emission scanning electron microscopy tomography, elemental imaging and deep learning-based microstructure quantification suitable to witness the structural and chemical progression of the silicon and SEI reformation upon cycling. The nanometer-sized SEI layer evolves into a micron-sized silicon electrolyte composite structure at prolonged cycles. Experimental-informed electrochemical modelling endorses an underutilisation of the active material due to the silicon electrolyte composite growth affecting the capacity. A chemo-mechanical model is used to analyse the stability of the SEI/silicon reaction front and to investigate the effects of material properties on the stability that can affect the capacity loss.

[1] Materials Center Leoben Forschung GmbH, A8700 Leoben, Austria. [2] WMG, University of Warwick, Coventry CV4 7AL, United Kingdom. [3] Carl Zeiss Microscopy GmbH, Oberkochen, Germany. [4] Varta Micro Innovation GmbH, A8010 Graz, Austria. [5]These authors contributed equally: T. Vorauer, J. Schöggl. ✉email: roland.brunner@mcl.at

For technology-relevant applications like renewable energy, e-mobility, or mobile electronic devices[1], silicon (Si)-based anodes represent one of the most promising approaches towards high-energy Lithium (Li)-ion batteries. The main advantages are the high theoretical specific capacity ($Li_{15}Si_4$ with 3578 mAh g^{-1}), a low price and the natural abundance[2,3]. However, a major disadvantage of silicon is that it undergoes high volumetric expansion (up to 300%) and contraction upon lithiation and delithiation[3–5], respectively, which results in an insufficient lifetime expectancy and strong capacity fading.

Several strategies have been developed in recent years to tackle the challenges with respect to the volume expansion of Si and associated issues leading to capacity fading[4–6]. Upscaling in an industrial setting remains challenging due to the lack of a complete understanding of the underlying structural and chemical degradation mechanism. The Si-based anode material conventionally features a porous matrix, and graphite particles[7] as well as the Si-based active material embedded in a carbon binder domain (CBD)[8–12]. Within the CBD, for instance, nano-sized particles[13–16] or carbon nanotubes[14,17–20] are dispersed within a polymeric binder[21,22] to ensure sufficient electrical conductivity. In principle, the ionic conductivity is determined by the porous network[15,23,24]. In general, the cycling stability is triggered by the interaction of the active material with the fluorine-containing electrolyte[3,25]. It becomes manifested in the formation of a solid interlayer between the active material and the CBD[3]. This interlayer formed within a single lithiation step is also referred to as the solid electrolyte interface (SEI)[8,26]. The initially formed layer usually shows a thickness of about 20 nm on the Si particle and is composed of fluorine (F), oxygen (O), carbon (C) and phosphorous (P)[3].

The volume rearrangement leads to mechanically induced cracking and gradual degradation of the active material[27], including CBD detachment resulting in the loss of electronic contact[2], but also affects the evolution of the SEI upon cycling as recently illustrated for Si-nano-sized wires[26] leading to progressive SEI growth on the formed void surfaces and finally to the destruction of the Si-nano wire´s integrity. However, the presented view in ref. [26] about the SEI evolution is very specific with respect to the cell configuration. In general, the configuration has a strong influence on the activation of the Si, which means that a half-cell configuration can lead to different results than a full-cell[28–31] in terms of structural and chemical development of the SEI. Notably, the SEI growth and the performance of the Li-ion battery can be also influenced by the charge/discharge current divided by the nominally rated battery capacity or C-rate[8,32]. Structural changes of the active material interface have been also observed in the full-cell configuration on different particle size length scales[33,34]. Those rearrangements have been hypothetically linked to the reformation of the SEI on the newly formed Si surface[33–35]. Nevertheless, experimental proof is still lacking on both the structural and chemical evolution at the Si interface upon cycling for a full-cell configuration. Such an understanding is crucial for improving anode material architectures suitable for industrial upscaling.

The anode covers different length scales ranging from the mm-range covering the whole electrode, to the anode microstructure, including graphite-, pore-, CBD- and Si-domains and ultimately to the nm-range incorporating, e.g. the immediate vicinity of the Si-domains or the single Si-particles[6]. The resolved features and their occurrence define the necessary volume of interest (VOI) for the subsequent analysis. Micro X-ray computed tomography (μ-XCT) and X-ray microscopy (XRM) provide possibilities to investigate the microstructure of electrode materials from mm to several hundreds of nm[36]. In particular, for battery research, an understanding of the correlated structural and chemical evolution

is essential. Gallium-focused ion beam field-emission scanning electron microscopy (FIB-FESEM) achieves a resolution with high material contrast of about 20 to 5 nm[36–38]. The possible field of view (FOV) lies in general at about 10 to 30 μm but can be extended by considering longer slicing times. Two-dimensional FIB-FESEM sliced microstructure images in correlation with energy dispersive X-ray spectroscopy (EDS) to detect O, C, Fe, Si[39] as well as time-of-flight secondary ion mass spectrometry (ToF-Sims) to detect Li in Li-ion batteries[40] has been demonstrated. Correlating the different experiments to cover the required length scales as well as the chemical range in industry-relevant full-cell configuration has not been done, to the best of our knowledge.

Here, we develop a correlated multi-scale workflow incorporating XRM, nano-FIB-FESEM and EDS-tomography combined with ToF-SIMS as well as utilise machine learning assisted volumetric image data segmentation, suitable to witness the structural and chemical modification upon cycling in Si-nanocomposite anodes, relevant for industrial upscaling. Ultimately the SEI evolves from a thin nm-sized layer in the first cycles, into a micron-sized silicon electrolyte composite (SEC) structure formed around the Si domains, leading to significant Li-trapping at prolonged cycles. The combination of deep learning-assisted segmentation and correlated chemical analysis allows the accurate assignment of the CBD and SEC. An intact Si interior is still present up to 300-cycles, exposing a capacity retention of about 70% with a C-rate of C/2.

Utilising microstructure-informed electrochemical modelling, we show that the capacity loss also goes with an underutilisation of the active materials due to the depletion of Li$^+$ within the grown SEC regions, upon cycling. Further, we discuss the SEC growth kinetics and the stability of the underlying Si/SEI reaction front. Based on the findings, we reveal how material properties govern the evolution of the Si/SEI interface and illustrate how an inhomogeneous stress configuration, e.g. due to a pore or a crack, in the vicinity of the Si/SEI reaction front can trigger an instability eventually impacting the SEC evolution.

Results

Correlated experimental structure and chemistry visualisation workflow. In this work, a full-cell configuration with a technology-relevant anode is used for the electrochemical cycling, see schematic in Fig. 1a. There is a different electrochemical activation at the Si interface in the full-cell configuration compared to the half-cell configuration since in the latter, the Si domains are flooded more intensely by the Li-ions. Therefore, differences with respect to SEI formation are expected[41]. The technology-relevant anode system utilised here, consists of a silicon (Si)-nanocomposite with amorphous silicon (a-Si) and crystalline iron-disilicide (c-FeSi$_2$) domains, embedded in a porous carbon binder domain (CBD) and graphite matrix[38]. A nickel-manganese-cobalt (NMC)-based cathode is used for the full-cell configuration. A lithium polyacrylate binder (LiPAA) and carbon black (CB) as the conducting agent is selected to define the CBD. The porous CBD network filled with the conducting agent facilitates the ion and the electrical conductivity.

In order to reveal the correlated structural and chemical evolution of the microstructure at the Si-nanocomposite interface from micro- to nanoscales, we develop a workflow (Fig. 1b–e) including XRM, FIB-FESEM tomography accompanied with EDS-tomography and ToF-SIMS. A convolutional neural network (CNN) model with U-Net architecture is used for the segmentation of the volumetric image data.

XRM is utilised on μm-scales to select a representative VOI for the detailed Si-nanocomposite interface analysis. As highlighted
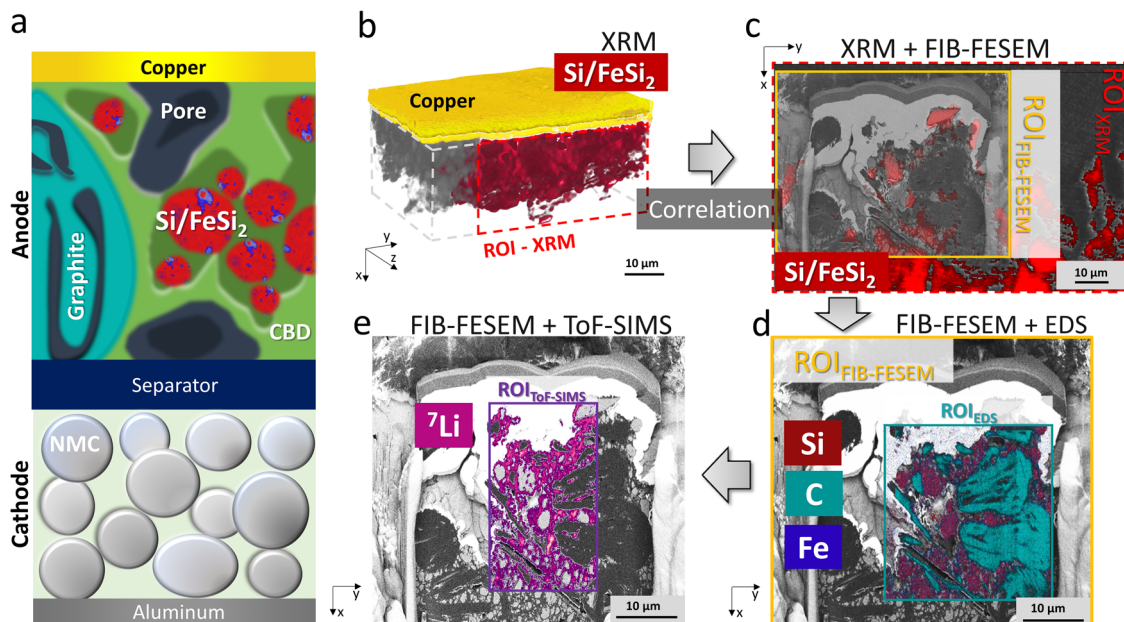
Fig. 1 Correlated experimental structure and chemistry visualisation workflow. a Schematic (not to scale) showing the full-cell configuration indicating the Si-nanocomposite anode, separator (dark blue) and a cathode, including the copper (gold) and aluminium (silver) current collectors. **b** XRM rendered 3D data of the silicon (Si)-nanocomposite anode (red) and copper current collector (gold) on top. This is a VOI chosen to include all the important phases. From here, the region of interest (ROI$_{XRM}$) highlighted with the red bounding box for the FIB-FESEM investigation is selected. The scale bar is 10 μm. **c** Representative XRM slice image in x-y-plane with a selected region for subsequent correlated FIB-FESEM tomography. FIB-FESEM image is projected (transparent) on top of the highlighted (red rectangular) region to show the correspondence. **d** Within the selected ROI$_{FESEM/FIB}$, the ROI for quasi-3D EDS is selected and measured every 250 nm (ROI$_{EDS}$). Overlay of the element count Si (red), Fe (blue) and C (cyan) onto the FIB-FESEM image reveals a good match for the a-Si/c-FeSi$_2$ compound and the graphite, respectively. **e** Similar to the EDS mapping, ToF-SIMS elemental composition mapping (ROI$_{ToF-SIMS}$) was also conducted on the last slice of the FIB-FESEM volume. Here, exemplarily the distribution of ^{7}Li is indicated, surrounding the a-Si/c-FeSi$_2$ compound.

in Fig. 1b, the rendered 3D XRM image resolves the Si-nanocomposite domains within the anode, including the copper current collector. The XRM is conducted due to its larger possible VOI in comparison to the limited VOI of FIB-FESEM. It enables the selection of a representative volume for the subsequent correlated 3D structural and chemical element characterisation on nm scales. The anode shows a multi-scaled microstructure, e.g. with pores or graphite with extensions up to a tenfold of a micron, as well as shows structural dimensions in connection to the Si-nanocomposites and interface region laying within the nm regime[39]. The XRM selection step is crucial to ensure a statistically relevant comparison between the VOI gained at high resolution for different cycling states. XRM provides a voxel size of $220 \times 220 \times 220$ nm^3 giving us the opportunity to achieve a large field of view with a volume of interest of $400 \times 31 \times 417$ μm^3. For the correlation of the XRM and FIB-FESEM tomography, the reconstructed X-ray dataset is aligned with the SEM sample surface in order to precisely correlate sample stage coordinates to the (subsurface) regions of interest identified in the X-ray tomogram (see method section). For the FIB-FESEM, we achieve a resolution of $12 \times 12 \times 12$ nm^3, see further details in the method section. We illustrate in Fig. 1c a FIB-FESEM slice image selected from the preceding XRM characterisation. The local correlation can be seen by projecting the FESEM slice image on the XRM-data.

Figure 1d, displays the correlation between the structural and chemical information, applying FIB-FESEM with EDS. The corresponding EDS mapping exemplarily maps the carbon (cyan), silicon (red) and iron (blue) distribution. For the correlated three-dimensional (3D-) EDS mapping, we gain a resolution of $50 \times 50 \times 250$ nm^3 and detect elements like Si, Fe, O and C, see further details in the method section.

Further, in Fig. 1e, the correlated ToF-SIMS mapping is used, illustrating exemplarily the distribution of ^{7}Li in the vicinity of the Si-composite. The ToF-SIMS provides 12×12 nm^2, and is sensitive to ^{16}O, ^{19}F and ^{6}Li as well as ^{7}Li. Hence, important information with respect to the structural and chemical evolution at the Si-nanocomposite interface can be gained upon cycling. This implies an understanding of the impact of the electrolyte, conductive agent, CBD and active Si-nanocomposite on the reformation process of the SEI or solid electrolyte composite (SEC) formation.

Supplementary Fig. 1 demonstrates the electrochemical cycling performance of the full-cell using the Si-nanocomposite anode at C-rates lower and equal to C/2 (see details in Method section). After 300-cycles, the cell capacity reveals a capacity fading of about 30% at C/2 with respect to the initial capacity.

Machine learning assisted analysis of the Si-nanocomposite anode degradation. The statistical analysis of the Si-nanocomposite electrode is crucial to understand the Si-interface evolution upon cycling. Figure 2 shows the machine learning (ML) assisted segmentation process of the FIB-FESEM tomography data. Representable VOIs for selected stages in the cycling process, i.e. for pristine, 3-cycles (formation step) and 300-cycles from top to bottom, respectively, are shown. The obtained grey value data indicates multiple heterogeneous material phases with complex geometric features ranging from μm to nm. Exemplarily cubes with a size of $7 \times 7 \times 7$ μm^3 each, are presented.

Conventional image analysis algorithms or manual labelling to segment the grey value data are highly labour intensive due to the high amount of image data. To achieve a sufficient segmentation
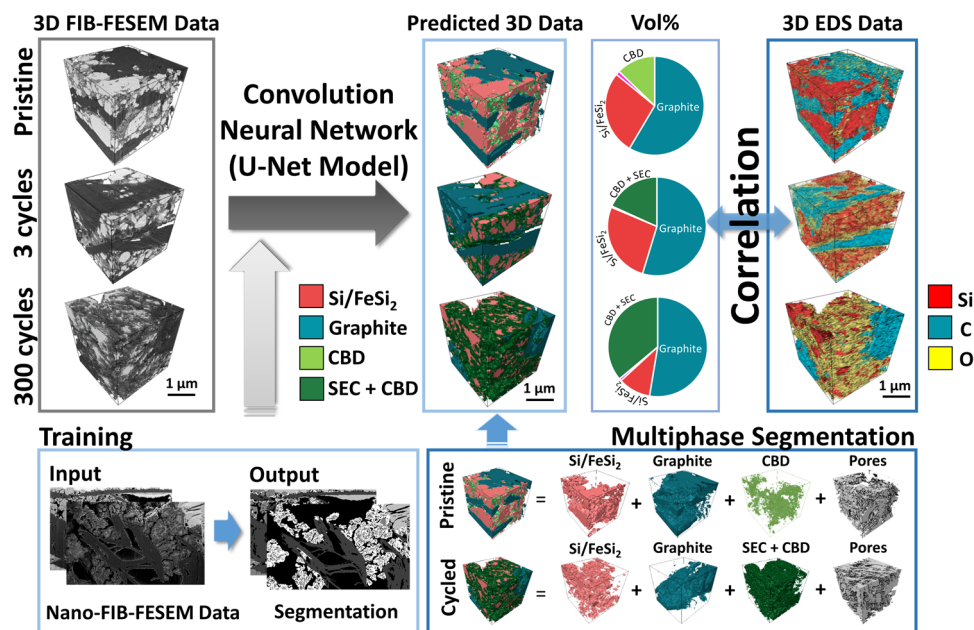
Fig. 2 Machine-learning assisted segmentation of the Si-nanocomposite electrode to reveal statistical information about the Si-nanocomposite degradation. 3D segmented volume of interest obtained from the FIB-FESEM-tomography data. left: From the top to the bottom, the samples pristine, after 3-cycles- (formation phase) and after 300-cycles (charging/discharging) are shown. The volume is about $7 \times 7 \times 7\ \mu m^3$ and the scale bar is $1\ \mu m$. bottom: To segment the FIB-FESEM 3D data accurately, the CNN-model was trained with labelled images from the FIB-FESEM measurements. middle: The CNN-based multiphase segmentation shows four phases with graphite (cyan), $Si/FeSi_2$ (red), pores (transparent or grey) and CBD (light green) for the pristine or SEC + CBD (dark green) for the cycled anode. Statistically relevant information with respect to modification of the volume fraction upon cycling is shown next to the predicted 3D data in a pie chart. Artefacts originating from the measurement are shown in magenta. The graphite content should be very stable throughout the cycling and is used as a reference to compare the volumes. With increasing cycling number, the core Si content is decreasing as the CBD + SEC volume fraction (dark green) is increasing. right: The correlated 3D-EDS elemental mappings indicate C (cyan), Si (red), O (yellow). The increase of the oxygen (yellow) with cycling in the 3D-EDS representation goes with an increase of the segmented SEC + CBD phase (dark green).

for the relevant phases, a trained convolutional neural network (CNN) was used with a U-Net[42] architecture, see also Supplementary Note 1. Although lithiation of the graphite phase cannot be neglected[39], the graphite content should be very stable in comparison to the active Si-nanocomposite and proximate interface throughout the cycling. The graphite phase is used as a reference to compare the volumes. According to the pie chart in Fig. 2, the volume percentage (Vol.-%) of the graphite does not significantly change. It also verifies the utilisation of the XRM as a preceding tool to select a representative VOI and to ensure a statistically relevant comparison between the VOI gained at high resolution for different cycling states.

Furthermore, due to the correlated approach, all emerging phases segmented by the CNN-model can be directly identified by the measured 3D elemental distribution shown in the EDS data.

The model is able to achieve satisfying segmentation results for all FESEM datasets into four different phases. The accuracy for the segmentation is about 90% (see Supplementary Note 1 for more information). For the pristine anode the graphite- (cyan), $Si/FeSi_2$- (red), the CBD- (light green) and pore- (grey) phase are depicted, which can be correlated with the carbon (C), silicon (Si) and oxygen (O) and EDS-non-detectable domain, respectively. Note, that within the 3D EDS data, the iron (Fe) distribution is not shown, therefore, see an exemplary 2D EDS slice image in Supplementary Fig. 2 for pristine, 3 cycles and 300 cycles. The colour-coding for the CNN prediction and the EDS elemental mapping is the same for better comparison.

A striking feature of the microstructure upon cycling concerns the gradual loss of the Si-volume fraction of about 50% from pristine to 300-cycles and the structural modification of the Si and its immediate vicinity illustrated by the ML segmentation.

The correlated EDS data supports the observed evolution of the microstructure upon cycling. The changes from the pristine to the 3-cycled sample in the immediate vicinity of the Si-composite are small but significant. A drastic modification of the microstructure is observed for the 300-cycled one. In particular, the oxygen contribution (yellow), depicted in the EDS data, is enhanced at the border of the Si-nanocomposite domain. Such behaviour has been illustrated in the literature[43]. Here, the observed gradual oxidation feature is not attributed to the native oxide layer on the pristine Si-composite but rather to the chemical reaction of the electrolyte with the Si.

Associated with the EDS findings, the ML-segmented FIB-FESEM data illustrates that with the decrease of the Si-nanocomposite phase (red) in the anode, an additional phase (dark green) is growing in the vicinity of the Si-nanocomposite domains upon cycling. This expanding phase depicted in the ML-segmented image data correlates primarily with the growing oxygen-related domain presented in the 3D-EDS data. Although the contribution of the phase marked in dark green at 3-cycles is 13 Vol.-%, it shows at 300-cycles 24 Vol.-%. This growing phase can most likely be associated with the reformation and destabilised growth of the SEI, growing stepwise with each lithiation process and gaining an extension in the upper nm- and μm-range. In the following discussion, we label this phase as the silicon electrolyte composite (SEC) phase, see also the discussion in Supplementary Note 2. Notably, even after 300-cycles, the Si-composite core is not overwhelmed by the SEI reformation and remains intact. For the segmentation based on the obtained FESEM grey value data, it is not possible to distinguish between the CBD and SEC, due to the lack of contrast.
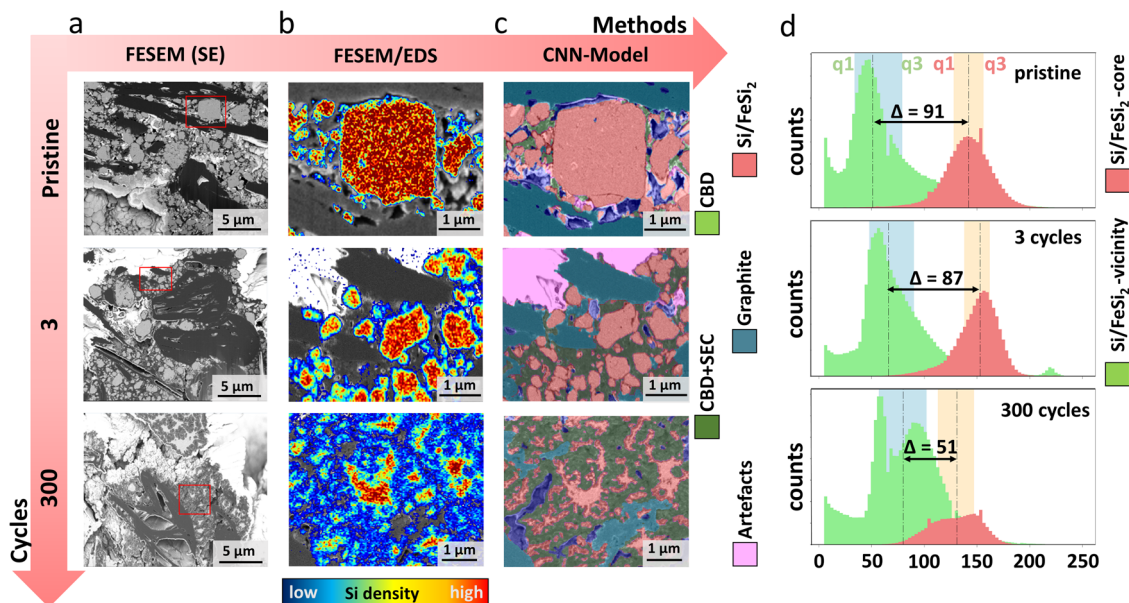
Fig. 3 Detailed FESEM and correlated EDS mapping to image the evolution of the Si-nanocomposite domain interface with cycling. a Cross-section of the last slice after the FIB-FESEM measurement. In the figure, the top, middle and bottom corresponds to the cross-section of the pristine, 3-cycled and 300-cycled sample, respectively. The change of morphology upon cycling is apparent in these overviews of the cross-sections. **b** Detailed EDS elemental mapping conducted at defined regions in the cross-sections with an increased amount of counts for more accuracy from pristine, 3-cycles and 300-cycles (from top to bottom). The silicon content distribution is highlighted in colour ranging from low (blue) to high (red). The increase of the low silicon content (blue) in the vicinity of the associated Si-core with respect to the increasing cycling number is obvious. **c** Segmentation obtained from the CNN-model superimposed onto the FESEM images with the same ROI as for the EDS. In red, the area associated with the Si/FeSi$_2$ domain or Si-core, in cyan the graphite particles, in light green the CBD for the pristine or in dark green the CBD + SEC for the cycled data and in magenta the artefacts e.g. deposited Pt (see Method section). The increase of the green phase with cycling is apparent. **d** Statistical information indicating the grey value distributions for the Si/FeSi$_2$ vicinity region (green) and the Si/FeSi$_2$-core region (red). The dashed line indicates the median of the distributions and the blue (vicinity) and orange (core) columns indicate the first (q1) and third (q3) quantiles for the distributions. From top (pristine) to bottom (300-cycles), the distance between the median for the vicinity and core regions is decreasing. That is, the average amount of silicon in the core regions is decreasing, i.e. the average Si-core is shrinking with increasing cycling leading to a growth of the SEC at the Si-interface.

Evolution of the Si-nanocomposite domain and interface. Further EDS element analysis in the discharged state with a longer acquisition time (see details in the method section) has been conducted in order to better highlight the evolution of the Si-nanocomposite and decomposition of the Si upon cycling due to the formation of the SEC. Figure 3a shows for different cycling states the FESEM cross-section and selected ROI used for the high-intensity EDS mapping, illustrated in Fig. 3b. The Si-distribution (blue means low Si density and red high Si density) from the EDS measurement is projected onto the FIB-FESEM image to investigate the distribution of Si within and in the vicinity of the Si domains. In addition, it can be compared to the ML segmentation in Fig. 3c, where Si is labelled red and the surrounding SEC-rich area is labelled green. The correlated structural and chemical evolution of the anode upon cycling becomes apparent.

In case of the pristine anode, a Si-nanocomposite core domain is observed see Fig. 3b. The core domain is illustrated by a high Si count (red) in the EDS data. This core region matches well with the ML-segmented domain in red obtained from the FIB-FESEM-data and associated with the Si-nanocomposite see Fig. 3c. According to the post-processed EDS data, only a thin region indicated by a low Si count (blue) at the Si-interface is observed.

For 3-cycles, Si-cores (red) with slightly irregular interface appearances as well as the leaking of the Si (blue) from the Si-core into the proximate domain (dark green), can be depicted (Fig. 3b, c). For 300-cycles, the FESEM, as well as the EDS images indicate a strong structural and chemical modification. The surface of the Si-nanocomposite domain becomes rougher. The lower

Si-content regions (blue) associated with the ML-segmented regions in dark green are spread over almost the entire domain. Only small Si-core domains are left after 300-cycles.

Furthermore, we quantify the evolution of the Si-nanocomposite core and its vicinity based on the grey value distribution obtained from the FIB-FESEM-data (see Supplementary Note 2 for details) for each sample independently. Figure 3d provides evidence that the average counts in the distribution associated with the Si-core (red) decrease upon cycling. In addition, the distances between the median (as a black dotted line) for the Si-vicinity (green distribution) and the median for the Si-core distributions (red distribution) are decreasing with cycling. The distance between the median values is independent of the relative position of the histograms. Therefore, the distances between different samples can be compared.

The distance between the Si-core and Si-vicinity for 3-cycles is slightly decreased when compared to the pristine anode. The grey values correspond to the atomic number of the elements. Thus, when Si mixes with CBD, the average atomic number of the assemblage mixes and this reduces the distance between the two material classes. The histogram plot after 300-cycles (bottom histogram plot), looks strongly different compared to the pristine and 3-cycled one. The analysed distance decreases drastically by about 45% from the pristine anode. The observed strong distance decrease and shrinking histogram for the core region, indicates a strong movement of Si from the Si-core region to its vicinity or SEC.

The notable evaluated gradual loss of the Si-volume fraction of about 50% from pristine to 300-cycles discussed in Fig. 2 can be
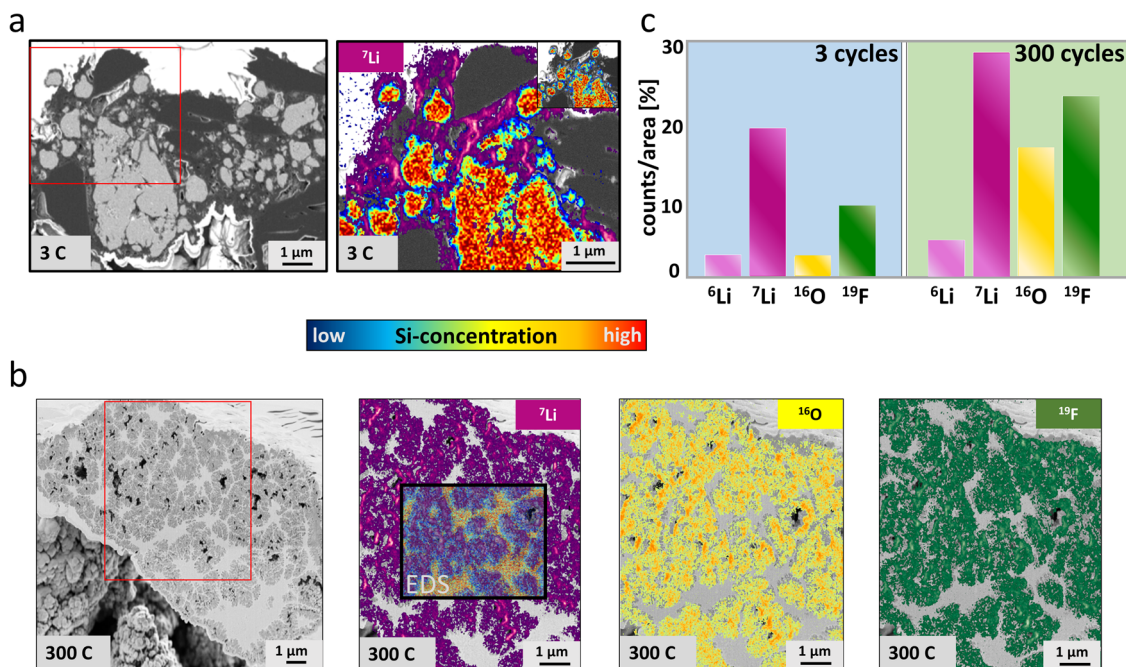
5

Fig. 4 Visualisation of the electrolyte permeation and SEC growth in the proximity of the Si-nanocomposite domains with cycling. Selected segmented FESEM image in correlation with post-processed EDS data and ToF-SIMS elemental mapping for 3-cycles and 300-cycles (discharged), respectively. **a** Three-cycles: On the left, we show the FESEM image and the selected ROI (red rectangle) for the correlated FESEM, ToF-SIMS and post-processed EDS analysis, which is illustrated on the right. The ^{7}Li-distribution is detected in the proximity of the intact Si-nanocomposite domain, where a low Si density is detected by EDS. The grown SEC with small Si-density (blue) and lithium (purple) as well as the present Si-core with high Si-density (red) and a non-significant lithium contribution, are forming a core-shell-like structure. See also the inset in the upper left corner just illustrating the EDS data projected on the FESEM image. **b** 300-cycles: FESEM image (left) with the selected ROI (red rectangle) used for the correlated structural chemical element analysis. Right hand, post-processed EDS mapping (transparent) is projected on a selected region to indicate the correlation between the Si- and Li-distribution. Even at 300-cycles, the core-shell structure seems to be preserved. Again, ^{7}Li (purple) is distributed in the proximity of the intact Si-nanocomposite domain associated with the grown SEC, where a low Si density (blue) is detected by EDS. Next to the right, oxygen (^{16}O) and fluorine (^{19}F) mapping are presented for the same ROI in yellow and green, respectively. Both elements are mainly detected in the grown SEC, as illustrated for the ^{7}Li (purple). **c** Evaluated counts for the elements ^{6}Li, ^{7}Li, ^{16}O and ^{19}F for the 3 and 300-cycled samples. The relative increase for the elements associated with SEI formation with increasing cycle number is apparent.

associated with the redistribution of the Si content from the Si-core domains into its proximate vicinity during the lithiation process. Former active Si might become less active due to the SEC formation and observed Si-redistribution, which can directly affect the capacity behaviour upon cycling.

Chemical element composition of the SEC. Complementary to the EDS elemental mapping, correlated ToF-SIMS in the discharged state has been conducted to study, in particular, the Li-distribution in context with the grown SEC within the anode (see also Supplementary Note 3). The method allows an understanding of the correlated structural and chemical evolution for the lithium ^{7}Li and ^{6}Li isotopes and for SEI signature isotopes, such as ^{19}F and ^{16}O, see Supplementary Fig. 4. Figure 4a illustrates the anode after 3-cycles including the FESEM image as well as the correlated EDS-Si (from blue to red)- and ToF-SIMS ^{7}Li-distribution (purple). Here, the observed ^{7}Li domain is still small. Figure 4b illustrates for 300 cycles the FESEM image and projected EDS-Si on top of the ^{7}Li-distribution. Here, enlarged ^{7}Li domains are located in the imminent proximity of the strongly altered Si-core, which can be associated with a low Si-count observed in the EDS data. To further illustrate the interaction of the electrolyte, we show the distribution of oxygen (^{16}O in yellow) and fluorine (^{19}F in green). Similar to the Li-mapping, ^{19}F and ^{16}O are mainly distributed in the region associated with a low Si-count or grown SEC region. The findings suggest that the breakdown of the Si-nanocomposite core forms additional SEC.

In addition, to study the chemical evolution of the SEC upon cycling further, we compare in Fig. 4c for 3- and 300-cycles the averaged values over several regions for the specific elements/isotopes. Here, ^{6}Li and ^{7}Li is increased by +167% and +151%, respectively. ^{16}O and ^{19}F show an increase of +546% and +155%, respectively. The different increase of the Li isotopes is most likely due to the segmentation of the small ROIs and the associated errors. Differences in the isotope diffusion rate would also be possible, but are not part of our consideration. The gained correlated structural and chemical information is a direct proxy for the used electrolyte[44] (LiPF$_6$) and also suggests the possible formation of Li$_x$Si, SiO$_x$ within the grown SEC[26]. Further, the formation of lithium-oxide cannot be neglected[45,46].

Determination of the SEC growth and CBD. The correlated structural and chemical analysis presented in this work provides the opportunity to investigate the expansion of the SEC during cycling. As demonstrated by the correlated EDS (Fig. 3) and ToF-SIMS analyses (Fig. 4), the chemical information obtained on Si, Li, O and F provides information on the distribution of the elements studied in the phase associated with the SEC. Note that due to limitations of the FIB-FESEM in resolution, it is not possible to detect a single SEI layer; rather, the continuous reformation of the SEI with cycling, which leads to extensive SEC growth in the proximity of the Si, is detected. By utilising the FIB-FESEM method and CNN-model analysis alone, a distinction between the CBD and SEC is not possible.
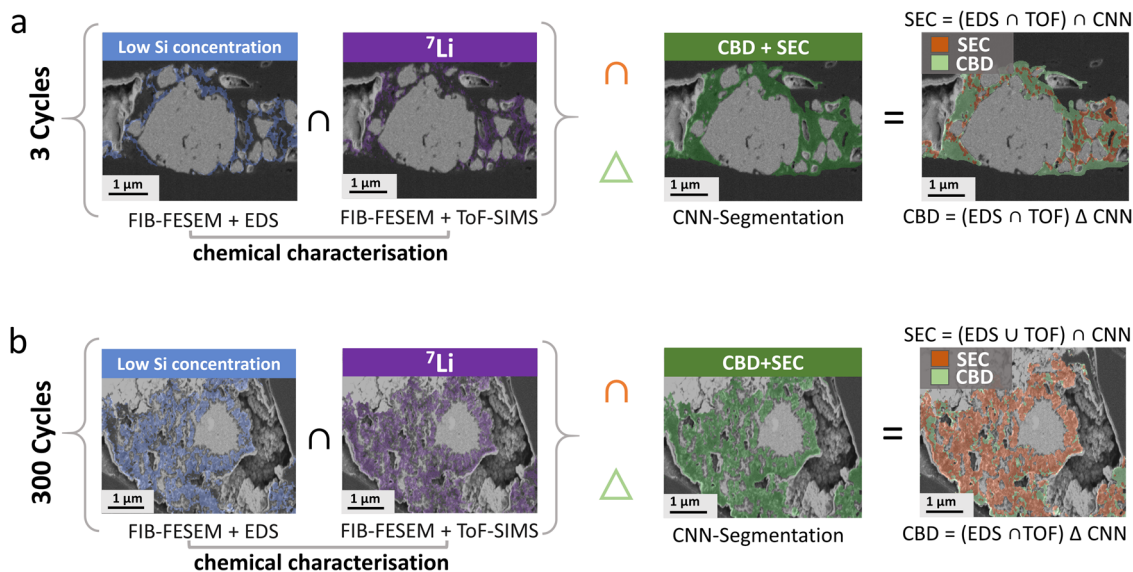
Fig. 5 SEC and CBD analysis based on the correlated FIB-FESEM, EDS and ToF-SIMS analysis. Workflow to distinguish between the CBD (light green) and the SEC (orange) domain based on the correlated EDS-, ToF-SIMS- and the CNN prediction analysis for **a** 3-cycles and **b** 300-cycles. The CBD + SEC is marked in dark green. The chemical data and CNN prediction are combined to obtain a common set of pixels. The extracted quantity can be associated with the SEC (orange). The symmetric difference between the generated intersected pixels and model prediction, gives the CBD (light green).

Notably, for the cycled anode, a comparison between Fig. 3b, c shows, that the EDS detection of the Si for regions in direct proximity around the core and the ML-segmented FIB-FESEM data associated with the CBD and SEC (dark green), do not fully agree. The discrepancy may be related to imperfect segmentation. However, the prediction of the CNN-model provides an accuracy of about 90% (see Supplementary Note 1 for more information). The CNN prediction for the CBD and SEC (dark green), see Fig. 3c, incorporates grey values laying between the large graphite particles (cyan), Si-nanocomposite domains (red), as well as pores (transparent) or the artefacts (pink). Note that the chemical association is a subset of the model prediction quantity. The detected low Si concentration from the EDS in Fig. 3c might be rather linked to the SEC, since it originates from the breakdown of the Si-nanocomposite forming around the still intact core domains. Further, the lithium content detected by the ToF-SIMS can be associated with trapped lithium within the SEC originating from the electrolyte $LiPF_6$. Nevertheless, the EDS- and ToF-SIMS data do not fully match. Measurement inaccuracy due to the lack of resolution cannot be neglected. We exclude the detection of the LiPAA-binder since no significant Li content is detected for the pristine anode. Each single method provides certain information in context to the SEC and CBD. However, the individual results are not fully conclusive due to analysis errors or measurement deficiencies.

To distinguish between the SEC and CBD, we utilise all three independent but correlated methods, i.e. EDS-, ToF-SIMS- and the CNN prediction, as illustrated in Fig. 5. Due to uncertainties in measurement and segmentation, the chemical methods and CNN prediction are combined to obtain a common set of pixels. The extracted quantity can be associated with the SEC. By taking the symmetric difference between the generated intersected pixels and model prediction, we obtain the quantity of pixels associated with the CBD, as shown in Fig. 5a, b for 3- and 300-cycles, respectively. On average, an increase of the SEC domain from about 65% to about 80% for 3- to 300-cycles can be extracted from this approach.

Chemo-mechanical modelling to understand the observed SEC growth. The conditions, which define the growth of the initial SEI, will have consequences on the further SEI reformation process,

which finally results in the formation of the SEC, see Fig. 3. An understanding of the growth stability on the SEI level is therefore crucial. Therefore, we investigate the stability behaviour of the SEI-Si reaction front using the approach developed in refs. [47–49] to gain a further understanding of the heterogeneous dendrite-like grown SEC microstructure shown in Figs. 3, 4. Commonly, unstable nature of the interface can lead to the emergence and growth of stress concentrations, which subsequently can lead to plastic deformation and damage. As shown in biological materials[50] the differences in the Young's moduli between different material layers help to stabilise the system by stopping cracks from forming or regulating the build-up of new layers. That is, the Young's moduli ratio, between materials present in the proximity of the reaction interface, may become a crucial parameter to consider when trying to enhance the anode performance. Here, the chemo-mechanical model, see also Supplementary Note 4, is based on the continuum solid mechanics framework. The growth of the SEI into Si is modelled as a stress-affected localised chemical reaction in a deformable solid body. The material is assumed to consist of the chemically untransformed solid phase (Si) and the chemically transformed solid electrolyte phase (SEI), which are separated by a non-stationary interface (or chemical reaction front), where the chemical reaction takes place. The approach is based on the concept of the chemical affinity tensor[51–53]. A schematic, Fig. 6a, displays the modelling region with the active particle (Si) with the outer SEI layer. Figure 6b shows stability zones in the parametric space for different elastic moduli of the phases as a function of chemical energy γ and transformation strain θ (Supplementary Fig. 5 shows further parametric variation). The combination of the elastic properties corresponds to different ratios (E_1/E_2) of Young's moduli of the Si (E_1) and the SEI (E_2) domains.

As shown in Fig. 6b, different stability scenarios are possible, depending, for instance, on the E_1/E_2 ratio—the equilibrium position can be stable, unstable or it might not exist (see Supplementary Note 4, where this case is shown and specific values of E_1 and E_2 are summarised). If $E_1/E_2 > 1$, a stable domain exists for relatively small γ and large θ and vice versa for $E_1/E_2 < 1$.

To visualise the growth kinetics of the stable and the unstable behaviours of the reaction front in time, separate modelling is performed. Two different scenarios, i.e. stable and unstable, are
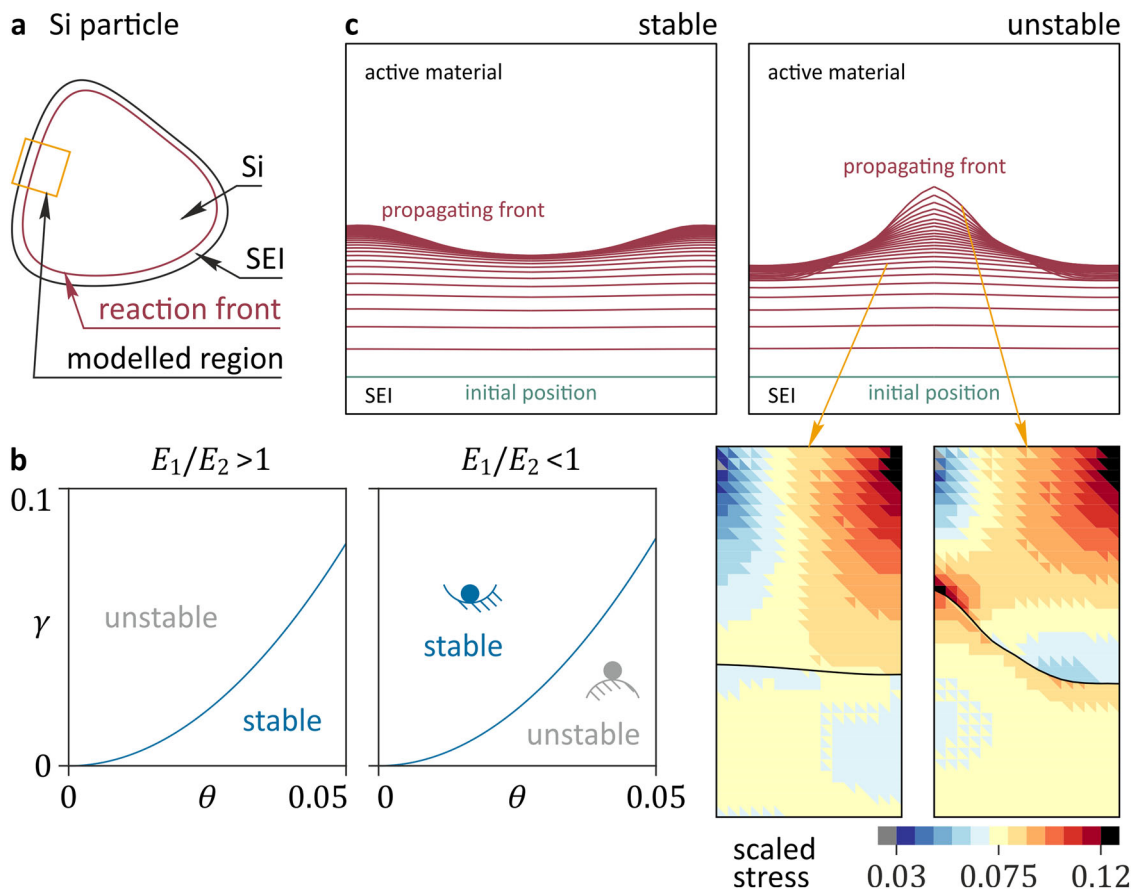
Fig. 6 Mechanical modelling of the SEI growth into Si. a Schematic of a Si particle surrounded by SEI and the reaction front in-between. **b** Stability behaviour of the planar reaction front between Si and SEI depending on the ratio of the Young moduli, chemical energy γ and transformation strain θ. **c** Time-evolution of the position of the reaction front in stable and unstable scenarios, and contour plots of the von Mises stress scaled by E_1 in the unstable case for two different time instances.

simulated using the Cut Finite Element Method (CutFEM) approach[54–57]. In the stable case (Fig. 6c, left), the reaction front slows down and approaches the equilibrium configuration. Here, only a small curvature is observed due to the inhomogeneity of the stress distribution caused by the applied boundary conditions. In the unstable case (Fig. 6c, right), the reaction front initially approaches the equilibrium position, but as it approaches it, a non-homogeneous stress distribution leads to a perturbation that starts growing exponentially due to the unstable nature of the interface.

The modelling results indicate that the physical stability of the planar reaction front depends on the ratio of Young's moduli of the phases (i.e. SEI and Si), which is a typical stability behaviour of phase boundaries and chemical reaction fronts in elastic solids[47,49]. For the problem studied here, there is a qualitative change in the stability regions in the parameter space when the moduli ratio goes past approximately 1. Furthermore, the behaviour of the interface between Si and SEI can shift between being stable and unstable if the chemical energy or the transformation strain changes. As indicated here, the consideration of Young's moduli present at the interface can be crucial and provide a qualitative explanation of the observed waviness of the grown SEC microstructure.

Experiment-informed electrochemical modelling—role of SEC on the capacity loss. To understand the mass transport, electrochemical behaviour, and Si-utilisation in context to the grown SEC, the discharge behaviour or anode electrode lithiation is

simulated in a simplified configuration utilising a half-cell configuration. The modelling is performed based on the retrieved segmented microstructure data, see Supplementary Fig. 6. The approach, see also Supplementary Note 5, will provide qualitative information in terms of a comparative study for 3- and 300-cycles applying the same set of parameters, see Supplementary Fig. 7, and with the SEC and CBD content being the only variance. The segmented microstructure obtained from the CNN-model, see Supplementary Fig. 6, as well as the SEC and CBD content defined by its ratio according to Fig. 5, can be used as an input parameter for electrochemical simulations. It enables the study of the impact of the SEC area on the capacity for different cycling states. The ratio SEC to CBD is about 65 to 35% and 80 to 20%, for 3-cycles and 300-cycles, respectively. For details and parameters used, please see Supplementary Note 5, Supplementary Fig. 7 and Supplementary Table 1–5 and the Method section.

Figure 7a–f illustrates the normalised Li⁺ concentration i.e. the ratio of the actual simulated Li⁺ concentration to the initial concentration of Li⁺ ($1000 \, \text{mol m}^{-3}$), as well as the electrolyte potential distributions across the SEC and proximate domains along with the state of lithiation of the active material domain at the end of the discharge process for 3-cycles and 300-cycles. It is evident that all variables of interest show heterogeneous gradients across the microstructures. Figure 7a, b depicts that the concentration of Li⁺ observes almost complete depletion across the SEC and proximate domains for both cycling states, with values varying between the order of $10^{-19} \, \text{mol m}^{-3}$, for inner SEC regions between the aggregated silicon domains, and
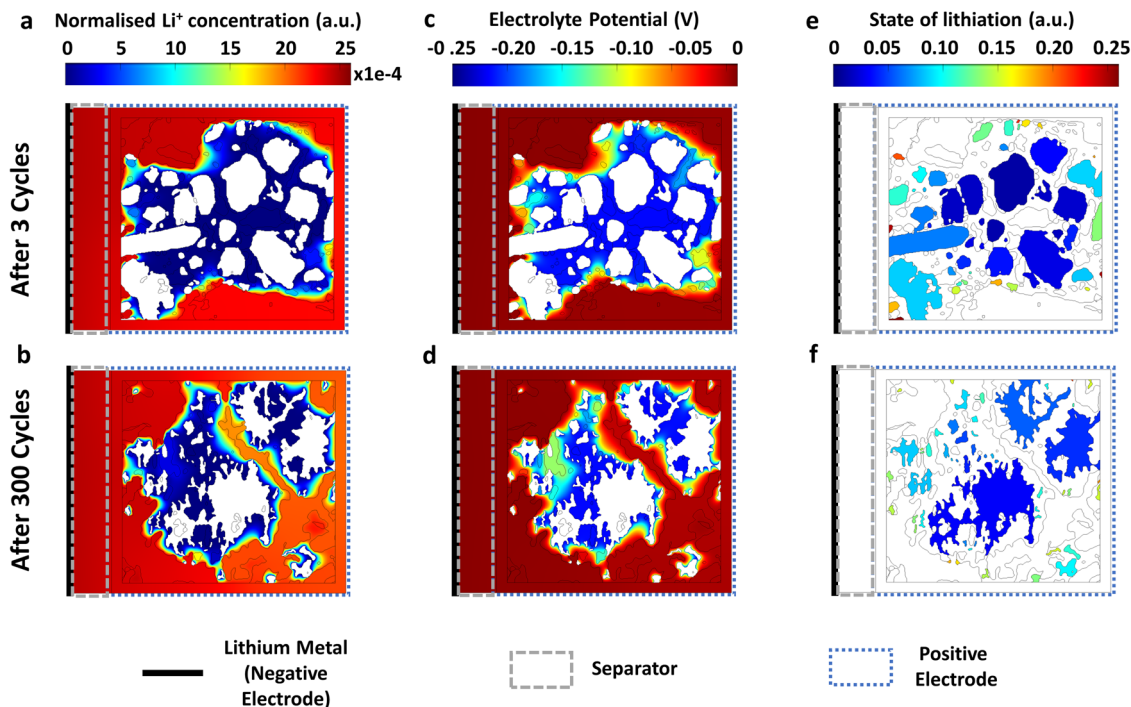
Fig. 7 Simulation results at the end of discharge potential profile for microstructures after 3- and 300-cycles. (**a**, **b**) Normalised Li$^+$ concentration and (**c**, **d**) electrolyte potential distribution across the separator, electrolyte and SEC domains for 3-cycles and 300-cycles, respectively. The normalised Li$^+$ concentration (unitless) is defined as the ratio of the actual simulated Li$^+$ concentration to the initial concentration of Li$^+$ considered in the model (1000 mol m^{-3}). The Li$^+$ concentration, as well as the electrolyte potential, show a significant difference between the electrolyte region and between the aggregated Si-region. (**e**, **f**) The state of lithiation for 3-cycles and 300-cycles, respectively. It displays a difference between the 3- and 300-cycled sample. The 300-cycled sample shows a lower lithiation rate than the 3-cycled one, implying the influence of cycling count on SEC growth and cell capacity reduction.

10^{-3} mol m^{-3} in the proximate domains. This significant difference can be attributed to a varying lithiation rate across the silicon-electrolyte and silicon-SEI interfaces due to the heterogeneous nature of the microstructure. The results go with the observations for the electrolyte potential distribution, see Fig. 7c, d. This is further reflected in the state of lithiation distribution (Fig. 7e, f) for both cycling states, where the outer silicon particles reach >10% while <5% for inner regions indicating poor utilisation of the active material. We affirm this observation when plotting the normalised histogram distribution of the state of lithiation across the active material region in the microstructure, shown in Supplementary Fig. 8a, b, with each bin counts on the horizontal axis representing 1% state of lithiation. The maximum state of lithiation reaches 30% for 3-cycles with a median value of 7.4 and 24% for 300 cycles with a median value of 5.1%. This underutilisation of active material observed for both states can be attributed to the depletion of active Li$^+$ present in the SEC region and its proximity. Note, that the trapped Li content in the SEC, as shown in Fig. 4b, is not considered in the modelling. The difference in the (median) state of Si lithiation between the 3-cycled and 300-cycled state of 2.3%, affirms the influence of cycling count on the growth of SEC and a reduction in the overall cell capacity. This reduction is also observed in the experimental electrochemical data illustrated in Supplementary Fig. 1. Furthermore, this is also reflected in the simulated discharge potential profile (see Supplementary Fig. 8c), which observes an earlier regression for 300-cycles than 3-cycles at lower discharge potentials (~0.4 V), indicating the continuous precipitation and growth of SEI products, which effectively hinders the contact surface area of the active material with the electrolyte.

The silicon regions, which observe a poor lithiation state, appear to be surrounded by regions that observe higher

negative (lowest) electrolyte potentials for both cycled states. This is reasonable considering the electrolyte potential is exponentially linked to the current density by the activation overpotential term in the Butler-Volmer expression, and any change in it will subsequently influence overall current density at the silicon particle surface (see Supplementary Note 5 for more details).

Discussion

SEI formation and subsequent reformation of the SEI in an industrial up-scalable cell configuration (Fig. 1a) leads to strong structural and chemical changes in the vicinity of the active Si material affecting the cell performance. The correlated measurement workflow presented here provides the possibility to cover the necessary length scales to gain sufficient structural and chemical information from the experimental data. According to the deep learning-based microstructure quantification, we evaluate a notable loss of the Si-volume fraction for the active Si nanocomposite core domains from pristine to 300 cycles by about 50%. After 300-cycles in the delithiated state, enlarged ^{7}Li domains are located in the vicinity of the strongly altered Si-core, indicating Li-trapping. In addition, a significant amount of oxygen and fluorine is detected, revealing the reaction of the fluorine-containing electrolyte with the active material and formation of Li$_x$Si and gradual oxidation of Si upon cycling[58] as well as suggests the formation of lithium-oxide[45].

The loss of Si in the core domains is explainable by the redistribution of the Si from the Si-core into its vicinity during the lithiation process. Formerly active Si becomes less active due to the growth of the solid electrolyte compound (SEC). The observed Si-redistribution directly affects the capacity behaviour during cycling. The experimentally informed electrochemical

modelling shows, in correlation with the chemical analysis, underutilisation of the active materials due to the depletion of the Li^+ concentration present in the grown SEC domains.

The present work shows the critical role of the interface formation at the active Si up to high cycling numbers, which is strongly different to graphite-based anodes[59]. Further, the cell configuration with respect to half-cell/full-cell is important considering the degradation of the Si material and SEI reformation process, see in comparison[26]. We observe a capacity retention of about 70% for C/2, exposing an intact Si-core up to 300-cycles. The nano-sized Si-composite material investigated here shows a more compact SEC growth along the active material interface than reported for micro-sized Si[33].

According to the experimental investigations and the chemo-mechanical modelling, we argue that the behaviour of the active material is influenced by the interface kinetics and the underlying material architecture. The interface behaviour is, in turn, influenced by the material properties, determining the subsequent formation of the SEC triggered by the reformation process of the SEI. One possible scenario is the unstable behaviour of the front, in which an inhomogeneous stress distribution will favour the further build-up of inhomogeneities, such as cracks or pores in the vicinity of the Si interface. Indeed, the modelling results indicate that the physical stability of the front depends on the ratio of the Young's moduli. Similar concepts have been shown elsewhere, e.g. refs. [47–50]. The understanding to restrain the inhomogeneous and uncontrolled build-up of the SEC is essential for improved energy storage solutions. The SEC formation has direct consequences on Si-degradation, Li-trapping and transport, as well as can lead to the emergence and growth of stress concentration and damage due to its unstable nature. Therefore, it will directly influence the capacity. The key to improved Si-based anodes will be the proper design of the active material and its structure e.g. utilising Si-alloys or Si-compounds, including the consideration of underlaying material parameters, e.g. the Young's modulus, etc. Well-designed active materials will help to control the interface kinetics during lithiation, stabilise the SEI formation and diminish its reformation as well as limit the extensive spatial SEC growth. That is, a functional design of the material architecture is needed for future Si-based anodes considering the underlying structure–property relationship[39,60,61] as a key ingredient.

Methods

Electrode preparation. A Hivis Mix Model 2P-03/1 mixer was used to produce the electrode paste. The electrode paste was coated using a semi-industrial Coatema Smartcoater. The electrodes were a composite of 50 wt% silicon-based active material 3 M L20772, ~1000 mAh/g), 41 wt% graphite (BTR918, ~372 mAh g^{-2}), 2 wt% carbon black (Super P) as conducting agent and 7 wt% LiPAA as a binder (made from Poly Acrylic Acid MW 450,000, Sigma Aldrich). They have an area capacity of 2.40 mAh c^{-1} m^{-2}. It consists of amorphous silicon (a-Si) with crystalline irondisilicide (c-FeSi$_2$) inclusions, and graphite. The active material contained in the L20772 powder is ~20% graphite, 25% a-Si and 55% c-FeSi$_2$ in weight.

Full-cell configuration. Pouch cells are prepared in a full-cell configuration utilising the prepared negative electrode, selected separator and positive anode. A schematic is presented in Fig. 1a. For the selected separator and electrolyte a celgard 2400 (monolayer polypropylene) and 1 mol L^{-1} lithium hexafluorophosphate (LiPF$_6$) in a fluoromethyl carbonate/ethyl methyl carbonate (3FEC/7EMC, v/v) binary solvent mixture with 2 wt% vinyl carbonate (VC) as SEI forming additive is used, respectively. For the cathode, a 2.0 mAh cm^{-2} (1/1/1) nickel–manganese–cobalt-oxide (NMC) is used. An aluminium and copper thin film is used as a current collector for the cathode and anode, respectively. The pouch cells were then opened in an argon-filled glove box, and the negative-electrode samples were taken away from the edges and sealed in aluminium laminated film pouches.

Electrochemical measurement. A Maccor battery tester series 4000 was used for the electrochemical measurements. The test cells were cycled with a charge/

discharge current rate (C-rate) of 0.5 C, whereas a rate capability check was performed at cycle 25 and subsequently every 100 cycles with C/10, C/5, C/2 and 2 C.

X-ray microscopy experiment and rendering of image data. Small samples were cut from the bulk material using scissors and glued to a sample holder suitable for analysis in both X-ray microscopes and FIB-FESEMs. X-ray microscopy measurements of sample C300 were performed on a Zeiss Xradia 620 Versa system. Projections of the sample were recorded in a two-stage magnification process that included optical magnification. The following acquisition parameters were chosen: An acceleration voltage of 60 kV, a beam current of 108 µA, a 40° objective, narrowing of the X-ray bandwidth by the LE1 filter, 220 nm effective pixel size, 360° rotation with exposure time of 23 s, and 3001 projections. The resulting tomography dataset was reconstructed with the ZEISS Scout-and-Scan Reconstructor software using the cone-beam method. Correlation between the XRM and the FIB-FESEM tomography is achieved using tracking marks positioned on the electrode sample surface and applying the Zeiss Atlas 5 package.

Field-emission scanning electron microscopy-energy dispersive x-ray spectroscopy. For improved electrical conductivity, samples were sputter coated with a ~20 nm Iridium layer in an Emitech sputter coater. The strong topography above the subsurface target regions of all three samples was levelled using suitable combinations of ion beam-induced platinum deposition normal to the FIB and FIB cuts parallel to the surface. The Zeiss Atlas 3D Analytics package was used to further prepare the sample surface with the characteristic Atlas 3D tracking marks, which were used during the experiments to dynamically correct for drifts of the sample both with respect to the FESEM beam (in x- and y-directions), and with respect to the FIB milling (in the z-direction). Images were acquired with a 12 nm pixel size at intervals of 12 nm. This shall ensure that anisotropic voxel sampling was avoided to enable precise measurements. During the collection of the imaging datasets, the FIB beam (30 kV/3 nA) and the FESEM beam (2.0 kV, 1.0 nA) were operated simultaneously. For EDS acquisition, FIB milling was paused and the FESEM ramped to analytical conditions (5 kV, 4 nA). The EDS elemental mapping was performed at slice increments that lead to non-isotropic voxels: Slices are separated by 250 nm, leading to 50 × 50 × 250 nm³ voxel sizes. At the chosen electron beam energy, 5 kV, according to SRIM calculations (http://www.srim.org/), the kV electron beam would sample approximately 200 nm sample thickness however, X-Ray emission would originate from a smaller depth, leading to undersampling. In order to avoid artefacts in that sense, we correlate each EDS elemental mapping with the corresponding FIB-FESEM image and matched the patterns in the images with one another, i.e. we used the elemental mapping for carbon (C) as a control for the segmentation for the graphite region that was based on the FIB-FESEM images. Total experiment times for 3D imaging and EDS summed up to ~29 h (Pristine sample), ~24 h (3-cycles sample) and ~23 h (300-cycles sample). The acquisition time per slice is estimated to be ~1.5 min. For the experiments described in Fig. 4, the estimated acquisition time was 5-6 min per map, until the drift of the sample became unstable.

Field-emission scanning electron microscopy-time of flight secondary ion mass spectrometry. Secondary ion mass spectrometry (SIMS) analyses were performed on the final cross-sections of the 3D EDS measurements, using a ToF-SIMS instrument (C-TOF, TOFWERK Company, Thun, Switzerland) connected to a Zeiss Crossbeam FIB-FESEM, see Supplementary Note 3. In order to achieve a near-normal incidence of the FIB beam on these FIB cross-sections, samples were tilted back from FIB normal to FESEM normal and rotated by 180 degrees. ToF-SIMS overview mappings were acquired on 20 × 20 µm² areas using a 10 kV, 10 pA FIB beam. Final ToF-SIMS mappings were done on 7 × 7 µm² areas using a 30 kV 10 pA FIB beam. Both overview and final mappings used a pixel resolution of 1024 × 1024 at 12.8 µs pixel dwell time, and a 4 × 4 binning.

Convolutional neural network for image analysis. A U-Net model from the Python library segmentation models[62] was used. The images and labels for the training of the model have been reshaped to 1248 × 1952 pixels, normalised to the first significant local maximum and divided by the standard deviation of the grey values for each image. The model was trained on an Nvidia Quadro M4000 (500 epochs) and an Nvidia Quadro RTX5000 (additional 500 epochs) GPU. Images have been labelled using the free software Ilastik. Artefact elements, namely the gallium deposits from the FIB beam, copper deposits from the FIB beam hitting the copper substrate as well as platinum for levelling the surface, which have been introduced with the FIB-FESEM measurement, has been determined by the correlated EDS. The EDS information is used to support the generation of the training data (see Supplementary Note 1). In order to provide comparability for the pristine, 3-cycled and 300-cycled sample, sub-volumes (7 × 7 × 7 µm³) with the condition of having a graphite content between 30–40 Vol.% have been selected. The graphite content is assumed to be very stable throughout the cycling and is used as a reference to compare the volumes.

Postprocessing of EDS data and ToF-SIMS. The EDS data was reconstructed using AZtec® Software from Oxford Instruments. The maps have been extracted as intensity images for the relevant elements: C, Si, O, Pt, Ga, Cu and Fe. The images have been thresholded (values >10% of max intensity) to remove the noise. The

ToF-SIMS images have been extracted from the measurement data using the TOF-SIMS Explorer® Software from Tofwerk AG and a Python script. Due to the measurement setup, the images were taken at an angle of ~54°. Therefore, the extracted images needed to be extended by this factor to get the scales correct with the FESEM and EDS images. (Supplementary Note 3) Afterwards, the images have been thresholded (values >10% of max intensity) in order to remove noise.

Visualisation and rendering of FESEM image data. The 3D visualisations for the FESEM image data have been made using Avizo® 3D. The correlations between the 2D images for the different measuring techniques have been made using Inkscape and/or python.

Correlation of image data. The Zeiss Atlas 3D Analytics package was used to further prepare the sample surface with the characteristic Atlas 3D tracking marks, which were used during the experiments to dynamically correct for drifts of the sample both with respect to the SEM beam (in x- and y-directions) and with respect to the FIB milling (in the z-direction).

Chemo-mechanical modelling. The chemo-mechanical modelling has been done using the framework based on the chemical affinity tensor[51–53]. In this approach, mechanical stresses affect the propagation of the chemical reaction front and can block it. At the equilibrium position, the stability analysis of the chemical reaction front has been carried out using the method developed in refs. [47–49]. The method consists of applying a perturbation to the interface and determining whether it grows or decays. In addition, the numerical simulations of the kinetics of the reaction front were carried out using the CutFEM method, recently extended to large deformations and chemo-mechanics problems[54,57]. More details on the problem formulation are provided in Supplementary Note 4.

Electrochemical modelling. The physics-based electrochemical model, based on the established Doyle–Fuller–Newman model[63], is developed using the electro-chemistry module on commercially available finite element software COMSOL Multiphysics v5.6. The geometries for as-received multi-phase two-dimensional microstructure images are reconstructed on MATLAB prior to their import into the finite element software. The model is simulated in a half-cell configuration with the lithium metal as an anode, 1 M LiPF6 (3:7 = EC:EMC) as the electrolyte and the as-received microstructure as a cathode. All parameters were sourced from COMSOL in-build material library and open literature. A fixed applied current with -4×10^{-6} A initiating from zero state of lithiation until the lower discharge cut-off potential of 0.2 V for both cycled states is used in the modelling. More details on the problem formulation are provided in Supplementary Note 5.

Data availability
All data that support the findings of this study are available from the corresponding author upon reasonable request.

Code availability
All code that support the findings of this study are available from the corresponding author upon reasonable request.

References
1. Hesse, H., Schimpe, M., Kucevic, D. & Jossen, A. Lithium-ion battery storage for the grid—A review of stationary battery storage system design tailored for applications in modern power grids. *Energies* **10**, 2107 (2017).
2. Mukanova, A., Jetybayeva, A., Myung, S.-T., Kim, S.-S. & Bakenov, Z. A mini-review on the development of Si-based thin film anodes for Li-ion batteries. *Mater. Today Energy* **9**, 49–66 (2018).
3. Schellenberger, M., Golnak, R., Quevedo Garzon, W. G., Risse, S. & Seidel, R. Accessing the solid electrolyte interphase on silicon anodes for lithium-ion batteries in-situ through transmission soft X-ray absorption spectroscopy. *Mater. Today Adv.* **14**, 100215 (2022).
4. Ko, M., Chae, S. & Cho, J. Challenges in accommodating volume change of Si anodes for Li-ion batteries. *ChemElectroChem* **2**, 1645–1651 (2015).
5. Gonzalez, A., Yang, N.-H. & Liu, R.-S. Silicon anode design for lithium-ion batteries: progress and perspectives. *J. Phys. Chem. C* **121**, 27775–27787 (2017).
6. Chae, S., Ko, M., Kim, K., Ahn, K. & Cho, J. Confronting issues of the practical implementation of Si anode in high-energy lithium-ion batteies. *Joule* **1**, 47–60 (2017).
7. Ryu, J., Hong, D., Lee, H. W. & Park, S. Practical considerations of Si-based anodes for lithium-ion battery applications. *Nano Res.* **10**, 3970–4002 (2017).
8. Attia, P., Das, S., Harris, S., Bazant, M. & Chueh, W. Electrochemical kinetics of SEI growth on carbon black: part I. Experiments. *J. Electrochem. Soc.* **166**, E97–E106 (2019).
9. Chevrier, V. L. et al. Evaluating Si-based materials for Li-ion batteries in commercially relevant negative electrodes. *J. Electrochem. Soc.* **161**, A783–A791 (2014).
10. Kierzek, K. Influence of binder adhesion ability on the performance of silicon/carbon composite as Li-ion battery anode. *J. Mater. Eng. Perform.* **25**, 2326–2330 (2016).
11. Kuruba, R. et al. Guar gum: structural and electrochemical characterization of natural polymer based binder for silicon-carbon composite rechargeable Li-ion battery anodes. *J. Power Sources* **298**, 331–340 (2015).
12. Tong, L. et al. Interface engineering of silicon/carbon thin-film anodes for high-rate lithium-ion batteries. *ACS Appl. Mater. Interfaces* **12**, 29242–29252 (2020).
13. Mahajan, V. & Bharj, R. S. Effect of particle size, surface area and conductivity of nano-carbon additives on deep discharge lead-acid battery. *Bull. Mater. Sci.* **44**, 52 (2021).
14. Zhang, R., Palumbo, A., Kim, J. C., Ding, J. & Yang, E. H. Flexible graphene-, graphene-oxide-, and carbon-nanotube-based supercapacitors and batteries. *Ann. Phys.* **531**, 1800507 (2019).
15. Gattu, B. et al. Scalable in-situ solid state reductive approach to reversible silicon/metal oxide/carbon based nanocomposite Li-ion anodes. *ECS Meet. Abstr.* **MA2017-01**, 26 (2017).
16. Chou, C. S., Tsou, C. H. & Wang, C. I. Preparation of graphite/nano-powder composite particles and applicability as carbon anode material in a lithium ion battery. *Adv. Powder Technol.* **19**, 383–396 (2008).
17. Zhu, S., Sheng, J., Chen, Y., Ni, J. & Li, Y. Carbon nanotubes for flexible batteries: Recent progress and future perspective. *Natl. Sci. Rev.* **8**, nwaa261 (2021).
18. Chen, X. & Ma, Y. Wearable lithium ion batteries based on carbon nanotubes and graphene. *Adv. Mater. Technol.* **3**, 1800041 (2018).
19. Sehrawat, P., Julien, C. & Islam, S. S. Carbon nanotubes in Li-ion batteries: a review. *Mater. Sci. Eng. B* **213**, 12–40 (2016).
20. De Las Casas, C. & Li, W. A review of application of carbon nanotubes for lithium ion battery anode material. *J. Power Sources* **208**, 74–85 (2012).
21. Li, S. et al. A review of rational design and investigation of binders applied in silicon-based anodes for lithium-ion batteries. *J. Power Sources* **485**, 229331 (2021).
22. Jing, J. et al. Study of commercial binders on the lithium storage performance of SiOx/G@C anode. *Mater. Chem. Phys.* **292**, 126797 (2022).
23. Pouraghajan, F. et al. The effects of cycling on ionic and electronic conductivities of Li –ion battery electrodes. *J. Power Sources* **492**, 229636 (2021).
24. Chen, C. et al. Interface aspects in all-solid-state Li-based batteries reviewed. *Adv. Energy Mater.* 11, 2003939 (2021).
25. Liu, K., Wang, Z., Shi, L., Jungsuttiwong, S. & Yuan, S. Ionic liquids for high performance lithium metal batteries. *J. Energy Chem.* **59**, 320–333 (2021).
26. He, Y. et al. Progressive growth of the solid–electrolyte interphase towards the Si anode interior causes capacity fading. *Nat. Nanotechnol.* **16**, 1113–1120 (2021).
27. Ratyński, M., Hamankiewicz, B., Krajewski, M., Boczar, M. & Czerwiński, A. The effect of compressive stresses on a silicon electrode's cycle life in a Li-ion battery. *RSC Adv.* **8**, 22546–22551 (2018).
28. Gutierrez, M. et al. Towards a better understanding of the degradation mechanisms of Li-ion full cells using Si/C composites as anode. *J. Power Sources* **533**, 231408 (2022).
29. Dupré, N. et al. Multiprobe study of the solid electrolyte interphase on silicon-based electrodes in full-cell configuration. *Chem. Mater.* **28**, 2557–2572 (2016).
30. Chevrier, V. L. et al. Design and testing of prelithiated full cells with high silicon content. *J. Electrochem. Soc.* **165**, A1129–A1136 (2018).
31. Sternad, M., Forster, M. & Wilkening, M. The microstructure matters: breaking down the barriers with single crystalline silicon as negative electrode in Li-ion batteries. *Sci. Rep.* **6**, 31712 (2016).
32. Heubner, C. et al. Diffusion-limited C-rate: a fundamental principle quantifying the intrinsic limits of Li-ion batteries. *Adv. Energy Mater.* **10**, 1902523 (2020).
33. Haufe, S., Bernhard, R. & Pfeiffer, J. Revealing the failure mechanism of partially lithiated silicon-dominant anodes based on microscale silicon particles. *J. Electrochem. Soc.* **168**, 080531 (2021).
34. Paul, N., Wetjen, M., Busch, S., Gasteiger, H. & Gilles, R. Contrast matched SANS for observing SEI and pore clogging in silicon-graphite anodes. *J. Electrochem. Soc.* **166**, A1051 (2019).

35. Ashuri, M., He, Q. & Shaw, L. L. Silicon as a potential anode material for Li-ion batteries: where size, geometry and structure matter. *Nanoscale* **8**, 74–103 (2016).

36. Scharf, J. et al. Bridging nano- and microscale X-ray tomography for battery research by leveraging artificial intelligence. *Nat. Nanotechnol.* https://doi.org/10.1038/s41565-022-01081-9 (2022).

37. Etiemble, A. et al. Evolution of the 3D microstructure of a Si-based electrode for Li-ion batteries investigated by FIB/SEM tomography. *J. Electrochem. Soc.* **163**, A1550–A1559 (2016).

38. Nan, N. & Wang, J. FIB-SEM three-dimensional tomography for characterization of carbon-based materials. *Adv. Mater. Sci. Eng.* **2019**, 8680715 (2019).

39. Vorauer, T. et al. Multi-scale quantification and modeling of aged nanostructured silicon-based composite anodes. *Commun. Chem.* **3**, 141 (2020).

40. Sui, T., Song, B., Dluhos, J., Lu, L. & Korsunsky, A. M. Nanoscale chemical mapping of Li-ion battery cathode material by FIB-SEM and TOF-SIMS multi-modal microscopy. *Nano Energy* **17**, 254–260 (2015).

41. Allgayer, F., Maibach, J. & Jeschull, F. Comparing the solid electrolyte interphases on graphite electrodes in K and Li half cells. *ACS Appl. Energy Mater.* **5**, 1136–1148 (2022).

42. Ronneberger, O., Fischer, P. & Brox, T. U-net: convolutional networks for biomedical image segmentation. in *Lecture Notes in Computer Science (including subseries Lecture Notes in Artificial Intelligence and Lecture Notes in Bioinformatics)* 9351 (2015).

43. Ratynski, M., Hamankiewicz, B., Buchberger, D. A. & Czerwinski, A. Surface oxidation of nano-silicon as a method for cycle life enhancement of Li-ion active materials. *Molecules* **25**, 4093 (2020).

44. Wheatcroft, L. et al. Visualization and chemical characterization of the cathode electrolyte interphase using He-ion microscopy and in situ time-of-flight secondary ion mass spectrometry. *ACS Appl. Energy Mater.* **3**, 8822–8832 (2020).

45. Munao, D., Van Erven, J. W. M., Valvo, M., Garcia-Tamayo, E. & Kelder, E. M. Role of the binder on the failure mechanism of Si nano-composite electrodes for Li-ion batteries. *J. Power Sources* **196**, 6695–6702 (2011).

46. Han, B. et al. Poor stability of Li2CO3 in the solid electrolyte interphase of a lithium-metal anode revealed by cryo-electron microscopy. *Adv. Mater.* **33**, 2100404 (2021).

47. Eremeev, V. A., Freidin, A. B. & Sharipova, L. L. Nonuniqueness and stability in problems of equilibrium of elastic two-phase bodies. *Dokl. Phys.* **48**, 359–363 (2003).

48. Yeremeyev, V. A., Freidin, A. B. & Sharipova, L. L. The stability of the equilibrium of two-phase elastic solids. *J. Appl. Math. Mech.* **71**, 61–84 (2007).

49. Morozov, A. Numerical and analytical studies of kinetics, equilibrium, and stability of the chemical reaction fronts in deformable solids. Thesis (Technical University of Berlin, 2021).

50. Fratzl, P. & Weinkamer, R. Nature's hierarchical materials. *Prog. Mater. Sci.* **52**, 1263–1334 (2007).

51. Freidin, A. B. Chemical affinity tensor and stress-assist chemical reactions front propagation in solids. In *ASME International Mechanical Engineering Congress and Exposition, Proceedings (IMECE)* (ASME, 2013).

52. Freidin, A. B., Vilchevskaya, E. N. & Korolev, I. K. Stress-assist chemical reactions front propagation in deformable solids. *Int. J. Eng. Sci.* **83**, 57–75 (2014).

53. Freidin, A. B. & Vilchevskaya E. N. Chemical affinity tensor in coupled problems of mechanochemistry. In *Encyclopedia of Continuum Mechanics*, (eds Altenbach, H. & Ochsner, A.) 264–280. (Springer Berlin Heidelberg, 2020).

54. Poluektov M. & Figiel L. A cut finite-element method for fracture and contact problems in large-deformation solid mechanics. *Comput. Methods Appl. Mech. Eng.* **388**, 114234 (2022).

55. Hansbo, A. & Hansbo, P. An unfitted finite element method, based on Nitsche's method, for elliptic interface problems. *Comput. Methods Appl. Mech. Eng.* **191**, 5537–5552 (2002).

56. Burman, E. & Hansbo, P. Fictitious domain finite element methods using cut elements: II. A stabilized Nitsche method. *Appl. Numer. Math.* **62**, 328–341 (2012).

57. Poluektov, M. & Figiel L. A numerical method for finite-strain mechanochemistry with localised chemical reactions treated using a Nitsche approach. *Comput. Mech.* **63**, 885–911 (2019).

58. Kumar, P. et al. Nano-architectured composite anode enabling long-term cycling stability for high-capacity lithium-ion batteries. *Small* **16**, 1906812 (2020).

59. An, S. J. et al. The state of understanding of the lithium-ion-battery graphite solid electrolyte interphase (SEI) and its relationship to formation cycling. *Carbon* **105**, 52–76 (2016).

60. Wijaya, A. et al. Multi-method characterization approach to facilitate a strategy to design mechanical and electrical properties of sintered copper. *Mater. Des.* **197**, 109188 (2021).

61. Sinojiya, R. J. et al. Probing the composition dependence of residual stress distribution in tungsten-titanium nanocrystalline thin films. *Commun. Mater.* **4**, 1–12 (2023).

62. Yakubovskiy, P. Segmentation models. *GitHub repository* (2019).

63. Fuller, T. F., Doyle, M. & Newman, J. Simulation and optimization of the dual lithium ion insertion cell. *J. Electrochem. Soc.* **141**, 1–10 (1994).

Author contributions

T.V. and J.S. performed the image analysis. R.B. planned and supervised the image analysis work. S.K. and B.F. fabricated and provided the samples. R.B., B.T. and S.S. planned and conducted the FIB-FESEM, EDS and ToF-SIMS measurements. T.V. and J.S. analysed the ToF-SIMS data with the supervision of R.B. B.F. performed the electrochemical measurements. Electrochemical simulations were performed by W.D.W and S.G.S. Chemo-mechanical simulations were performed by L.F. and M.P. All authors discussed the results and commented on the paper. R.B. wrote the paper with support from T.V. and J.S. and discussions mainly with B.F., B.T., L.F., M.P., S.G.S. and W.D.W.

Competing interests

The authors declare no competing interests.

Additional information

Supplementary information The online version contains supplementary material available at https://doi.org/10.1038/s43246-023-00368-1.

Correspondence and requests for materials should be addressed to R. Brunner.

Peer review information *Communications Materials* thanks the anonymous reviewers for their contribution to the peer review of this work. Primary Handling Editors: Jet-Sing Lee and Aldo Isidori. A peer review file is available.

Reprints and permission information is available at http://www.nature.com/reprints

Publisher's note Springer Nature remains neutral with regard to jurisdictional claims in published maps and institutional affiliations.